minerals

MDPI

*Article*

# The Effect of Curing under Applied Stress on the Mechanical Performance of Cement Paste Backfill

**Yue Zhao [1,2,3], Abbas Taheri [3,*], Murat Karakus [3], An Deng [3] and Lijie Guo [1,2,*]**

[1] Beijing General Research Institute of Mining and Metallurgy, Beijing 100160, China; zhaoyue@bgrimm.com
[2] National Centre for International Research on Green Metal Mining, Beijing 102628, China
[3] School of Civil, Environmental and Mining Engineering, The University of Adelaide, Adelaide 5005, Australia; Murat.Karakus@adelaide.edu.au (M.K.); An.Deng@adelaide.edu.au (A.D.)
* Correspondence: abbas.taheri@adelaide.edu.au (A.T.); guolijie@bgrimm.com (L.G.)

**Abstract:** After placing the Cement Paste Backfill (CPB) slurry in mined cavities underground, during the setting and hardening processes, the weight and hydrostatic pressure of the upper-layer CPB slurry applies an axial load over the bottom-layer CPB materials, which is called the self-consolidation of CPB slurry. Due to this phenomenon, the mechanical properties of in situ CPB could be considerably different from laboratory results. Hence, it is crucial to understand the effect of self-consolidation behaviour on the mechanical properties of backfill material. This paper presents an experimental study on the impact of axial applied stress ($A_s$) during curing, which represents the various self-consolidation conditions and curing times on the mechanical properties of CPB material prepared using the tailings of a copper mine in South Australia and a newly released commercially manufactured cement called Minecem (MC). A curing under pressure apparatus (CPA) is designed to cure CPB samples under axial applied stress. The equipment can apply and measure axial load during curing and measure the passive lateral stress due to axial load which represents the horizontal stresses at a certain depth of CPB stope on the retaining structure. The prepared samples with axially applied pressure during curing were tested under uniaxial and triaxial compressive loading conditions. Microstructural tests by scanning electron microscopy (SEM) were also used to study the fabric evolution in response to various applied stresses during curing. Overall, the increase in $A_s$ during curing leads to higher resultant CPB peak strength and stiffness under uniaxial and triaxial compression tests. For instance, a sample cured under 3.6 MPa axial load for 28 days demonstrates a uniaxial compressive strength (UCS) value of five times more than a sample cured under atmospheric curing conditions. Passive lateral stress was measured during the curing period and was representative of underground barricade stress. Furthermore, during curing, the axial applied stress changed the initial CPB pore structure after placement. With the increase in applied stress, the stress compressed CPB samples at the macroscale, leading to much smaller pores or cracks prior to the hydration process. At an early stage, the increase in UCS due to axial applied stress mainly arises from a dense microstructure caused by the compression of tailings and cement particles. With the increase in curing time, the observation also shows that a CPB matrix with fewer pore spaces may improve the hydration progress; hence, the influence of axial applied stress becomes more pronounced in long-term UCS.

**Keywords:** cemented paste backfill; Minecem; self-consolidation; axial applied stress; mechanical performance; passive lateral stress

**Citation:** Zhao, Y.; Taheri, A.; Karakus, M.; Deng, A.; Guo, L. The Effect of Curing under Applied Stress on the Mechanical Performance of Cement Paste Backfill. *Minerals* **2021**, *11*, 1107. https://doi.org/10.3390/min11101107

Academic Editor: Rafael Santos

Received: 26 August 2021
Accepted: 8 October 2021
Published: 9 October 2021



## 1. Introduction

The mining industry generates a large quantity of tailings every year during the extraction of valuable minerals from ore [1,2]. Conventionally, flotation tailings are deposited using surface tailing storage facilities. This may damage the local environment and

mine site geotechnical stability, and cause economic problems [3–8]. In the past few decades, with the awareness of sustainable mining, the use of backfill has been constantly increasing. The waste tailing as a base material of backfill will be used to fill mined cavities underground to improve underground mine geotechnical stability rather than stored in dumps. In this way, it provides an alternative disposal method for the tailings. The cost of environmental protection will be mitigated by minimising the adverse effects associated with tailing disposal [3,9–16].

In the 1980s, a new backfill method—Cement Paste Backfill (CPB)—was first used. The CPB is a mixture of mine tailings, a low proportion of binders, and a relatively low proportion of water, forming a high-density slurry (similar to a paste) that obtains a non-settling character, allowing facile pumping into underground mined stopes [17,18]. Ordinary Portland cement (PC) is the binder often implanted in CPB, while industrial low cementitious solid wastes such as fly ash, metallurgical slag, silica fume and waste gypsum can also be used as supplementary cementitious materials in mine backfill. Hence, its use reduces the operating cost related to cementitious material and provides a new solution for industrial waste utilisation [6,19,20]. Compared with other backfill methods, i.e., rock fills and hydraulic fills, the paste backfill has higher mechanical performance, lower operating costs, and the benefit of disposing tailings underground [13–16]. For these reasons, CPB has been increasingly applied worldwide over the past few decades to fill underground cavities. The properties that influence CPB's mechanical performance have been broadly studied in previous studies, i.e., the particle size distribution and chemical composition of tailings, binder type and content, water content and chemical composition, temperature, and drainage condition during curing [13–15,21–30].

Numerous researchers have indicated that when using the conventional sample preparation method (moulds), the determined data in laboratory testing underestimate the actual in situ mechanical performance of a CPB sample with the same mix recipe and curing period [31,32]. The backfill material's self-weight consolidation behaviour after placement is one major factor that may contribute to the underestimation of CPB's in situ strength. In an in situ condition, mine fill stopes are enormous, with heights of at least 20 m. After placing the CPB material in the stope, during the setting and hardening processes, the weight and hydrostatic pressure caused by the CPB material applies an axial load over the CPB paste from the upper layer to the bottom layer of the stope, which may facilitate the consolidation of early aged bottom layers. In this study, this consolidation is called self-consolidation. With the increase in backfill depth and CPB's weight in the stope, the bottom layers of CPB are cured under pressure [33,34]. Some in situ measurements of cemented paste backfill show that laboratory-made CPB samples underestimate 50% to 200% of the CPB strength compared with the strength obtained by cored specimens from an in situ backfill stope [34–36].

To determine the effect of the self-consolidation behaviour of backfill material, Benzaazoua et al. and Yilmaz developed a system called CUAPS (Curing under Applied Pressure System)[37,38]. With the use of this CUAPS, Yilmaz et al. applied a maximum 400 kPa stress on CPB samples during curing and found the uniaxial compressive strength (UCS) of the consolidated samples cured for 7, 14, 28 days (4.5% binder content) are 52.4%, 54.4%, 51.8% higher than unconsolidated CPB samples [33,39,40]. However, the maximum applied pressure during curing was limited to 400 kPa. A case study on in situ measurements of cemented paste backfill shows that for a height difference of 4 m, the peak vertical stress measured could be as high as 200kPa [32]. Furthermore, le Roux et al. also indicate that if the induced stress due to mining activity is considered, the vertical stress within the CPB stope could be doubled, and the modelling of vertical stress shows a 600 kPa vertical stress for a stope of only 10 m [31]. Hence, 400 kPa stress does not describe CPB samples' real in situ condition as the maximum depth of CPB stope could be as high as 100m. Additionally, Yilmaz et al. only studied the physical evolution during the consolidation of CPB material and summarised the increment of UCS after self-consolidation mainly due to the refinement of the pore structure due to axially applied stress [33,39],

while the influence of axially applied stress on the hydration process of binders in CPB material has not been studied. In addition, during the process of backfilling, the access drives should be barricaded with retaining walls. The failure of this structure could cause injuries and fatalities and lead to mine closures [41–43]. In the design of backfill barricades, it is essential to understand the stresses on the retaining walls. When applying axial stress over CPB samples during curing, passive lateral pressure occurrences could represent the horizontal stresses at a certain depth of the CPB stope on the retaining structure. Hence, it is essential to understand how the passive lateral stress occurred while applying axial stress during the curing of CPB samples.

This present study investigates the influence of various axially applied pressures using a newly developed slag-blended cement for three different curing times in confined and unconfined loading conditions. A novel curing under pressure system is designed and developed to place axially apply stress ($A_s$) on the CPB samples during curing and measure the passive lateral stress that occurs. Axial stress was applied to the CPB sample during curing up to 150 m self-weight height. Uniaxial compressive and triaxial tests were carried out to evaluate the effect of self-weight curing on the strength, brittleness, and stiffness of the CPB samples that are cured for a different period under different confining pressure conditions. Microstructural tests by scanning electron microscopy (SEM) were also used to study the fabric evolution (hydration process) in response to various stresses applied during curing. Passive lateral stress due to applied axial pressure during curing was also measured to investigate the passive pressure on the barricade during backfill placement.

## 2. Raw Materials

### *2.1. Tailings Material*

The processed tailings used in the present study were sourced from a copper–gold underground mine in South Australia. Table 1 illustrates the physical and mechanical properties of the tailings, determined as per the relevant ASTM standards [26–28].

**Table 1.** Physical properties and chemical composition of the used tailings.

| Physical Properties | Value | Chemical Component | Mass Percentage (%) |
|---|---|---|---|
| Specific gravity, $G_s$ | 2.61 | $SiO_2$ | 38.27 |
| Fines, <75 μm (%) | 38.6 | $Fe_2O_3$ | 37.70 |
| Fine sand, 0.075–0.425 mm (%) | 55.2 | $Al_2O_3$ | 7.19 |
| Medium sand 0.425–2 mm (%) | 6.2 | $K_2O$ | 2.33 |
| Liquid limit, $w_L$ (%) | 19.2 | Ca | 0.81 |
| Plastic limit, $w_P$ (%) | 13.1 | Mg | 0.75 |
| Plasticity index, $I_P$ (%) | 6.1 | Ti | 0.56 |
| Optimum water content, $w_{opt}$ (%) | 8.7 | $Na_2O$ | 0.07 |
| Maximum dry unit weight, $\gamma_{dmax}$ (kN/m$^3$) | 20.2 | Other | 12.32 |

Characterisation results indicate that the tailings sample has a specific gravity $G_s$ of 2.61. Grain size analysis showed that this tailings material contains 38.6% of fine grains <75 μm, 55.2% fine sand, and 6.2% medium sand. The Atterberg limits were determined using an experimental procedure adapted from standard ASTM D4318 [44]. The mine tailings showed only slight plasticity, with a liquid limit of 19.2% and plastic limit of 13.1. These tailings can be categorised as nonplastic silt according to the Unified Soil Classification System. The standard Proctor compaction test carried out by ASTM D698 [45] indicated an optimum water content of 8.7% and a maximum dry unit weight of $\gamma_{dmax}$ = 20.2 kN/m$^3$.

The chemical composition mainly consists of silicon dioxide ($SiO_2$) and iron oxide ($Fe_2O_3$), with mass fractions of 38.27% and 37.70%, respectively.

### *2.2. Binder and Water*

A commercially manufactured slag-blended cement (Minecem, MC) specifically developed for underground mine backfilling applications was used as the binder. The chemical composition of MC is shown in Table 2. Minecem is a slag based cement that contains 50% granulated blast furnace slag, 20% Portland cement clinker, <15% cement kiln dust, 5–7% natural gypsum, <7% limestone, and other mineral additives. With the use of this Minecem at 3% binder dosage, the CPB sample results in 519 kPa unconfined compressive strength (UCS) after 28 days' curing. The UCS of CPB samples containing 3% and 4% Ordinary Portland cement after 28 days' curing were only 363.5 and 425 kPa for the same tailings used [26], while when replacing 4% dosage of PC to 3% of MC in the mine, the use of MC reduces the backfill slurry yield stress from 210.7 Pa (4% PC) to 178.5 Pa (3% MC). Hence, the use of MC mitigates both the binder usage and the energy required to ensure adequate pipeline transport of CPB [28].

The mixing water used was mill process water, which was sourced from the same mine in South Australia. The chemical composition of mill process water is presented in Table 2. The mill process water was characterised as a neutral substance with a 7.5 pH value [26–28].

**Table 2.** Chemical composition of MC and mine-processed water.

| Minecem Chemical Component | Mass Percentage (%) | Processed Water Component | Value (mg/L) |
|---|---|---|---|
| Granulated blast furnace slag | 50 | $Cl^-$ | 5800 |
| Portland cement clinker | 20 | $SO_4^{2-}$ | 2400 |
| Cement kiln dust | <15 | $NO_3^-$ | 6 |
| Natural gypsum | 5–7 | $Na^+$ | 3800 |
| Chloride, $Cl^-$ | <8 | $Ca^{2+}$ | 480 |
| Limestone | <7 | $K^+$ | 380 |
| Sulfur trioxide, $SO_3$ | <4 | $Mg^{2+}$ | 280 |
| Crystalline silica | <1 | | |

## 3. Experimental Program

### *3.1. Curing Apparatus*

#### 3.1.1. General Setup

The Curing under Pressure Apparatus (CPA) was developed to mimic the in situ pressure over a CPB sample in stope during curing and was developed based on the system previously designed and manufactured by Benzaazoua et al. and Yilmaz [37,38]. In Benzaazoua and Yilmaz's system, a single convoluted air spring, which only provides a maximum of 600 kPa, was used, while an ENERPAC hydraulic pump (ENERPAC, Milwaukee, WI, USA) providing up to 6 MPa of axial stress was used in this new Curing under Pressure Apparatus, as shown in Figure 1. After applying the axial load through the hydraulic pump, the load can then be translated through the centre plate to a PVC piston on top of the CPB sample during curing. The load cell records the axially applied load and can be translated to axial pressure using the sample's top surface area. Once the load level reaches the prescribed value, six screw nuts above and below the centre plate should then be tightened to keep the continuous axial pressure during CPB curing.

Furthermore, compared to Benzaazoua and Yilmaz's system, as shown in Figure 1, a specially designed double-layer mould was placed on the base plate. The inner part of the mould comprised three 120-degree arches to form a circle of 5 mm thickness with an inner radius of 63 mm. After the curing process, the inner part could be extracted from the outer layer with the CPB sample to prevent damage during demolding. The outer layer of the mould is a rigid transparent metal round tube with 1 mm-thickness. With this thickness, the deformation of the outer mould could easily be measured, and the passive lateral

stress that occurred during curing could be detected through the deformation of the outer mould, which will be discussed in Section 3.1.2.

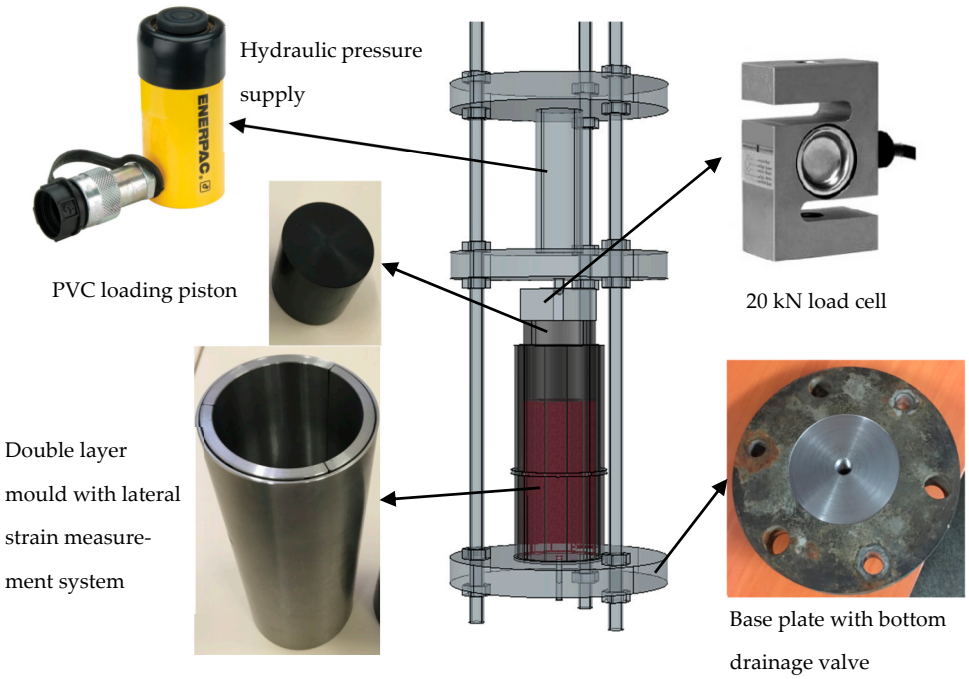


**Figure 1.** Curing under pressure apparatus (CPA).

### 3.1.2. Passive Lateral Stress Measurement

As shown in Figure 2a, the outer mould is designed to be as thin as possible to deform under the influence of passive lateral stress due to axial applied stress during curing. The deformation of the outer mould was measured by two lateral foil strain gauges (FLA-30–11 manufactured by Tokyo Sokki Kenkyujo Co., Tokyo, Japan) attached directly to the surface of the outer mould in the lateral direction. A UCAM-10B (manufactured by Kyowa Electronic Instruments Co., Ltd., Tokyo, Japan) data logger was used to record the measured axial applied stress and lateral deformation of the steel mould during curing.

Three calibration tests were performed to define the relationship between the lateral deformation of the steel mould ($\varepsilon_L$) and the passive lateral stress ($\sigma_L$) resulting from axial pressure. Lateral stresses were applied through a closed-loop servo-controlled testing machine (Instron-1342, Instron®, Norwood, MA, USA) at a 0.05 mm/min loading rate. During the calibration tests, the deformation of steel moulds was controlled to be less than 80 μm, making sure the steel moulds underwent elastic deformation. Figure 2b illustrates the recorded lateral stress ($\sigma_L$) and lateral strain ($\varepsilon_L$) of the steel moulds, where the number of data points recorded was reduced for better visualisation. The measured steel mould deformation during curing could then be used to calculate the passive lateral stress which occurred due to $A_s$.

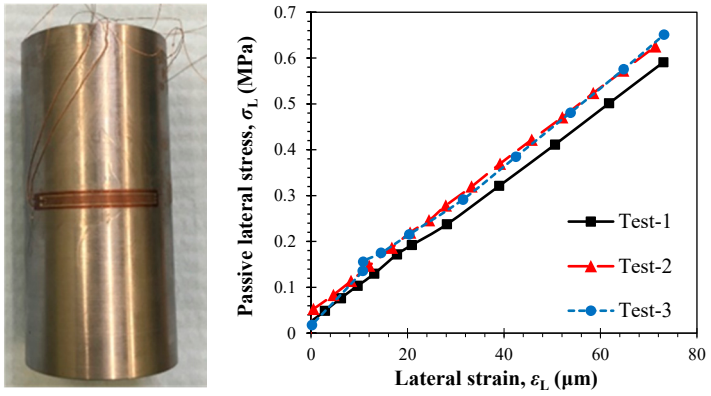


**Figure 2.** Passive lateral stress measurement. (**a**) Strain gauge on the steel mould (**b**) Calibrated passive lateral stress–lateral strain relations for steel moulds (number of points reduced).

As shown in Figure 3, the CPA is used to estimate the actual curing condition of CPB at various depths in a backfill stope under a specific self-weight consolidation pressure during curing. Figure 3 displays the layout and position of an ideal specimen without considering the filling sequence. During the test, passive stress in the lateral direction occurred when applying axial self-weight consolidation pressure in the axial direction. If no arching effect occurs, where there is no stress redistribution to the surrounding rock mass, the passive lateral stress measured could represent the barricade stress at the same level.

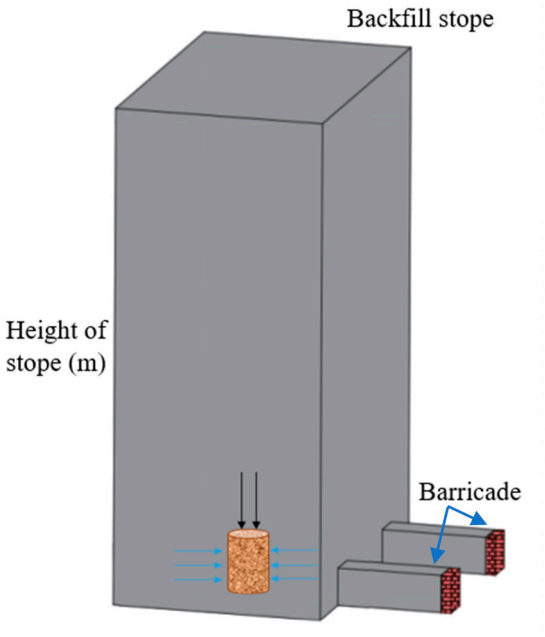


**Figure 3.** Layout and position of an ideal specimen.

### *3.2. Sample Preparation*

According to the mine's requirement, a Minecem content of 3% by total dry weight and solid content of 77% by total weight ought to satisfy standard strength criteria for cemented paste backfills that are used in mining applications. Hence, only one binder content (3% MC) and one solid content (77% solid content) were used in this study. The

tailings and MC were initially mixed in dry form using a bakery mixer. Then, the appropriate amount of processed mined water was added to make the slurry reach 77% solid content and mixed for about 5 min. The resultant slurries were poured into the cylindrical double-layer moulds (Section 3.1.1.; measuring 63 mm in diameter and 130 mm in height). The PVC loading piston was then placed into the mould to prevent any leakage of slurry during curing after applying axial pressure. One sample using pure tailings without any binder addition and any applied pressure was prepared for the SEM test as a reference state [26–28].

Four different axial stress levels were selected (0 MPa,1.2 MPa, 2.4 MPa, and 3.6 MPa), representing four different overburden dead loads for various depths (CPB under 0 m, 50 m, 100 m, and 150 m stope) of CPB in a large backfill stope; further, three different curing periods were selected (7 days, 14 days, and 28 days). Hence, a total of 12 curing designs were prepared in this study.

For ease of presentation, the following coding system is used to designate the various curing designs:

$$A_aT_b$$

where $A_a$ indicates a MPa axial applied stress during curing; $T_b$ indicates b days of curing.

Six samples were prepared from the same batch for each curing design for two uniaxial compressive loadings (to repeat the test) and four triaxial compressive loadings.

### *3.3. Uniaxial and Triaxial Compression Tests*

According to the ASTM C39 standard [46], uniaxial compression tests were carried out on CPB samples using a closed-loop servo-controlled testing machine (Instron-1342, Norwood, MA, USA) with a loading capacity of 250 kN. The machine loading rate for both uniaxial and triaxial compression tests was set to 0.1 mm/min.

CPB samples prepared under different curing conditions were subjected to triaxial compression tests described in the ASTM D2664 standard [47] under four different confining pressure values (0.5 MPa, 1 MPa, 2 MPa, 4 MPa) using a 63.5 mm HTC Hoek triaxial cell as the confining apparatus.

For ease of presentation, the following coding system is used to designate the various testing conditions:

$$A_aT_bC_c$$

where $A_a$ indicates a MPa axial applied stress during curing, $T_b$ indicates b days of curing, and $C_c$ indicates c MPa of confining pressure.

### *3.4. Scanning Electron Microscopy Analysis*

Microstructural tests by scanning electron microscopy (SEM) were also used to study the fabric evolution (hydration process) in response to various applied stresses during curing. The SEM images were performed using a Philips XL20 scanning electron microscope with a resolution of 4 μm and a maximum magnification ratio of 50,000×.

A total of nine mix designs, including one sample using pure tailings without any binder addition as a reference state and eight samples consisting of four different $A_s$ at two curing periods (7 and 28 days), were examined ($A_{0,\ 1.2,\ 2.4,\ 3.6}T_{7,\ 28}$).

## 4. Results and Discussions

### *4.1. Uniaxial Compressive Strength*

Uniaxial compressive strength (UCS) is one of the major indexes used to evaluate the mechanical performance of CPB. Figure 4a–c illustrates the stress–strain curves for samples under 12 curing conditions in the unconfined compressive test. With the same 7-day curing time—$A_aT_7$, where a = {0, 1.2, 2.4, 3.6}—while the applied stress increased, the UCS resulted in 476.5 KPa, 659.1 kPa, 751.3 kPa, and 1097.5 kPa, respectively. CPB samples

provided a UCS increase of 38.3%, 57.6%, and 130.2% for 1.2 MPa, 2.4 MPa, and 3.6 MPa applied stress at 7 days of curing (Figure 4a); 29.6%, 105.4%, and 206.1% for 1.2 MPa, 2.4 MPa, and 3.6 MPa applied stress after 14 days of curing (Figure 4b); and 60.3%, 234.5%, and 390.7% for 1.2 MPa, 2.4 MPa, and 3.6 MPa applied stress after 28 days of curing (Figure 4c), respectively. Overall, as shown in Figure 4d, the increase in $A_s$ during curing leads to the higher resultant peak strength during curing at the same curing time. With the increase in curing time, especially after 28 days, the influence of $A_s$ during curing becomes more pronounced; UCS increased by 390.7% when comparing samples $A_0T_{28}$ and $A_{3.6}T_{28}$. Moreover, when the stress applied during curing increases, the influence of curing time on CPB UCS becomes more pronounced as well.

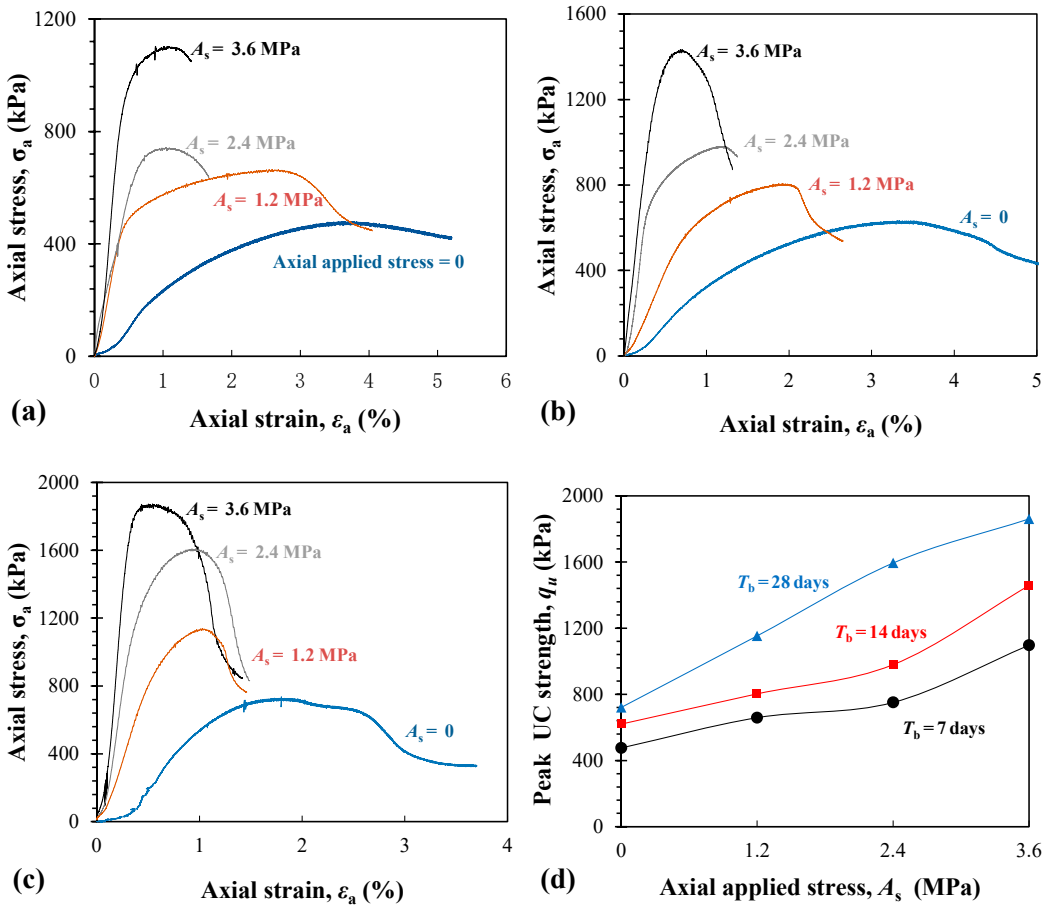


**Figure 4.** Uniaxial compression test results for CPB under the different $A_s$ (**a**) stress–strain relations for 7-day-cured samples, (**b**) stress–strain relations for 14-day-cured samples, (**c**) stress–strain relation for 28-day-cured samples, and (**d**) peak strength vs. axial applied stress.

The axial strain at failure ($\varepsilon_f$) for all samples prepared is displayed in Figure 5a. The strain at failure is an essential index of CPB's ductility. As shown in Figure 5a, the axial strain at failure strongly depends on the curing period and $A_s$. With the increase in curing time and $A_s$ during curing, the samples become more brittle. However, unlike the trend of UCS, when the applied stress increases (i.e., 2.4 MPa and 3.6 MPa), the influence of curing time on sample ductility becomes less sensitive.

The elastic stiffness modulus ($E_{50}$) values for all prepared samples were measured and displayed in Figure 5b. For samples cured for 7 days, with the increase in $A_s$, $E_{50}$ increased from 12.5 MPa to 23.6 MPa, 64.2 MPa, and 106.5 MPa, respectively. Similar to the trend of UCS, the development of $E_{50}$ attributed to the increase in $A_s$ and curing period and the mutual influence of $A_s$ and curing time on $E_{50}$ was enhanced with the increase in $A_s$ and curing time.

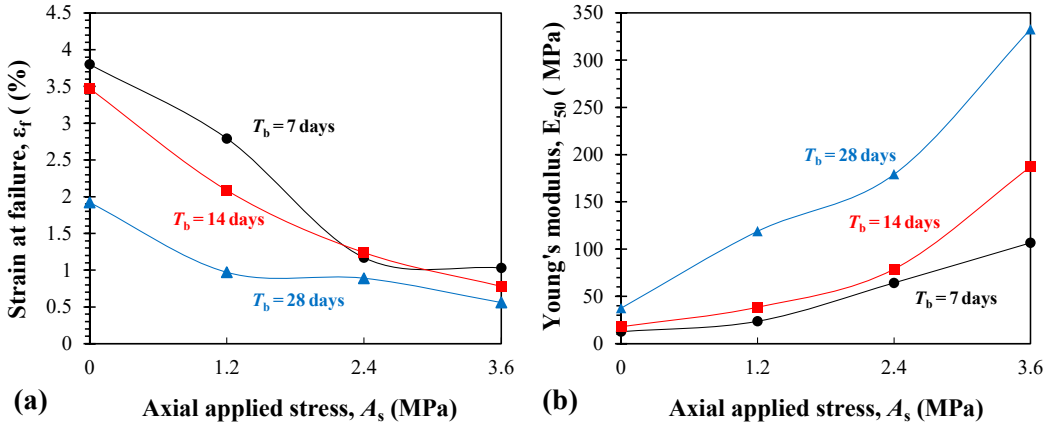


**Figure 5.** Uniaxial compression test results. (**a**) Peak strain at failure. (**b**) Young's modulus for 3% MC-CPB under the different depths of upper portion overburden (axial applied stress).

### *4.2. Triaxial Compression Strength*

The stress–strain curves for all samples prepared obtained from the triaxial compression tests under four different confining pressures ($\sigma_3$ = 0.5 MPa, 1 MPa, 2 MPa, 4 MPa) are shown in Figures A1–A3 in the Appendix A.

The stress–strain locus for all CPB samples under the triaxial test did not exhibit a detectable peak point with a rise and fall behaviour, as the CPB is a soft material that presents a strain-hardening effect under triaxial compression. Hence, the deviator stress and strain energy at 5% axial strain (i.e., $q_5$ and $E_{5;}$ at $\varepsilon_a$= 5%), respectively, were selected to represent the material's strength and toughness under triaxial compression.

Figure 6 illustrates the variations of $q_5$ against confining pressure for the samples $A_aT_b$, where a = {0, 1.2, 2.4, 3.6} and b = {7, 14, 28}. At any given axially applied pressure and curing period, the greater the confining pressure, the higher the $q_5$. As typical cases, for CPB samples cured for 7 days under zero axial applied stress, when the confining pressure were 0.5 MPa, 1 MPa, 2 MPa, and 4 MPa, the resultant $q_5$ values was 1081.3 kPa, 1169.7 kPa, 1212.8 kPa, and 1588.5 kPa, respectively. The sample $A_0T_7$ provides q5 values at increments of 8.1%, 12.1%, and 46.9% for 1 MPa, 2 MPa, and 4 MPa confining pressures compared to $q_5$ for 0.5 MPa confining pressure. With the increase in axial applied stress during curing, the influence of $q_5$ value under various confining pressure became more pronounced. For instance, the sample $A_{2.4}T_7$ resulted in $q_5$ = 1727.9 kPa, 2348.3 Pa, 3246.9 kPa, and 5439.2 kPa, for confining pressure of 0.5 MPa, 1 MPa, 2 MPa, and 4 MPa, respectively. The $q_5$ increments are 35.9%, 98.3%, and 209.7% for confining pressure of 1 MPa, 2 MPa, and 4 MPa.

However, for any given $A_s$ during curing, an increase in curing time leads to a less notable increase in $q_5$ under various confining pressures. The sample $A_{2.4}T_7$ resulted in a 209.7% increase between 4 MPa and 0.5 MPa confining pressure, while the 14 and 28 days curing samples led to lower increments of 152.6% and 143.8% between the 4 MPa and 0.5 MPa confining pressures.

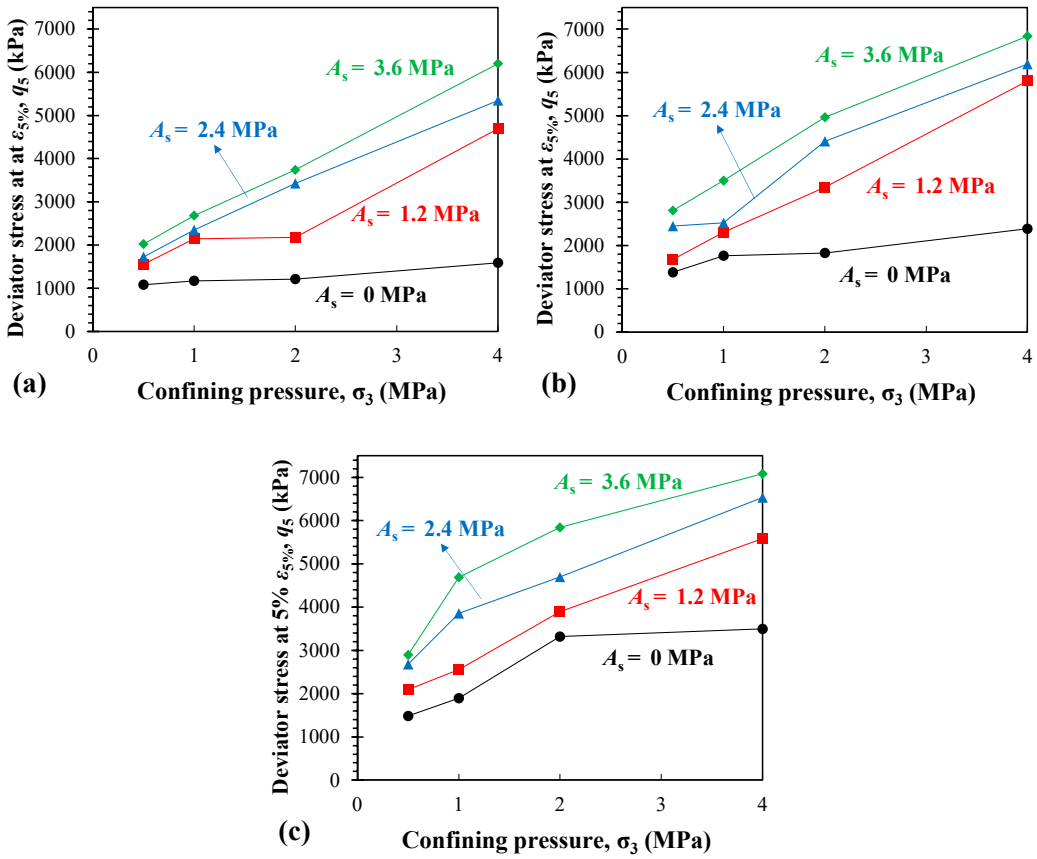


**Figure 6.** Deviator stress at $\varepsilon_a$ = 5% for CPB under different axial applied stresses. (**a**) 7 days curing, (**b**) 14 days curing, (**c**) 28 days curing.

### *4.3. SEM Observations*

Scanning electron microscopy (SEM) analysis was used to identify the influence of applied stress on the microstructural properties of CPB samples. Figure 7 presents the SEM micrographs for the sample prepared by pure tailings material under zero applied stress as a reference state. The SEM micrographs of CPB samples cured for 7 days under zero applied stress and 3.6 MPa applied stress are displayed in Figure 8a,b. In Figure 7, many large pores and cracks form a loose matrix and are observed in the pure tailings samples' SEM micrograph. After curing for 7 days, the CPB sample under zero applied stress with 3% MC had a less visible network of micropores and cracks than the pure tailings sample. This includes the finer particles in the binder, and the hydration products fill in the voids. With the presence of water, tailings, and calcium-rich binders such as MC, the primary hydration reaction is strongly time-dependent [27,29,48]. The major hydration products are Calcium–Silicate–Hydrates (C–S–H), in the form of poorly crystalline fibres to the reticular network; Calcium hydroxide ($Ca(OH)_2$), in the form of hexagonal-prism crystals; and ettringite (AFt), in the form of needle-shaped prismatic crystals, which encourage solidification and flocculation of the tailings particles and, hence, enhance strength performance [29,49–52]. Under the influence of applied stress during curing, the microstructure of sample $A_{3.6}T_7$ in Figure 8b contains much smaller and far fewer pores or cracks. Moreover, comparing samples $A_0T_7$ and $A_{3.6}T_7$, the applied stress during curing did not seem to influence the hydration of calcium-rich binders such as MC in the short term.

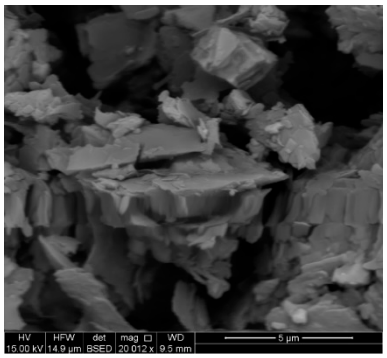

**Figure 7.** SEM micrographs for the tested samples prepared by pure tailings.

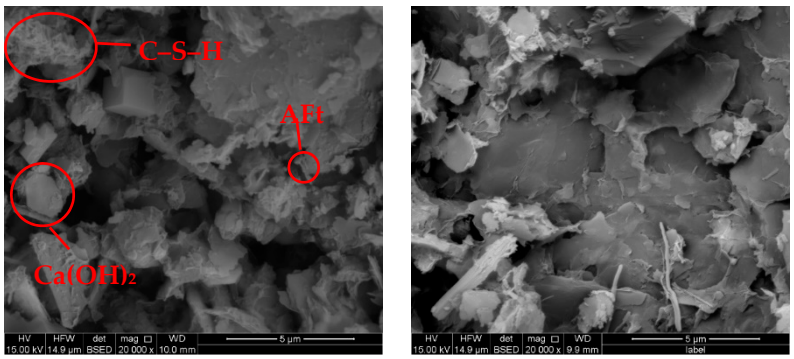


(**a**) (**b**)

**Figure 8.** SEM micrographs for the tested samples cured for 7 days. (**a**) $A_s$ = 0 MPa, (**b**) $A_s$ = 3.6 MPa.

Figure 9 illustrates SEM micrographs for the CPB samples at 28 days curing under various axially applied stresses during curing (0 MPa, 1.2 MPa, 2.4 MPa, 3.6 MPa). For sample $A_0T_{28}$ (Figure 9a), the observed pores and cracks are relatively high; this is similar to the micropore matrix of sample $A_0T_7$, where more hydration products are visible in the sample $A_0T_{28}$ micrograph than in the sample $A_0T_7$ micrograph. With the increase in $A_s$ during curing, the SEM micrographs of samples $A_{1.2}T_{28}$ and $A_{2.4}T_{28}$ illustrate a more densely structured matrix with less visible pore-spaces and fewer intercracks. For sample $A_{3.6}T_{28}$ in Figure 9d, a dense matrix with an edge-to-face flocculated structure was observed, and more hydration products—especially the C–S–H calcium silicate hydrate phase—were visible in the SEM micrograph. In general, the higher the applied axial stress during curing, the greater the number of developed cementation products formed in the long term (28 days). This fits the observation in Section 4.1, where CPB samples provided a UCS increase of 38.3%, 57.6%, and 130.2% for 1.2 MPa, 2.4 MPa, and 3.6 MPa applied stress at 7 days curing (Figure 4a); 29.6%, 105.4%, and 206.1% for 1.2 MPa, 2.4 MPa, and 3.6 MPa applied stress at 14 days curing (Figure 4b); and 60.3%, 234.5%, and 390.7% for 1.2 MPa, 2.4 MPa, and 3.6 MPa applied stress at 28 days curing (Figure 4c), respectively. The increase in UCS due to axial applied stress at an early age is mainly from dense microstructure caused by the compression of tailings and cement particles. With the increase in curing time, the dense microstructure could improve the long-term hydration; hence, the influence of axial applied stress becomes more pronounced in long-term UCS.

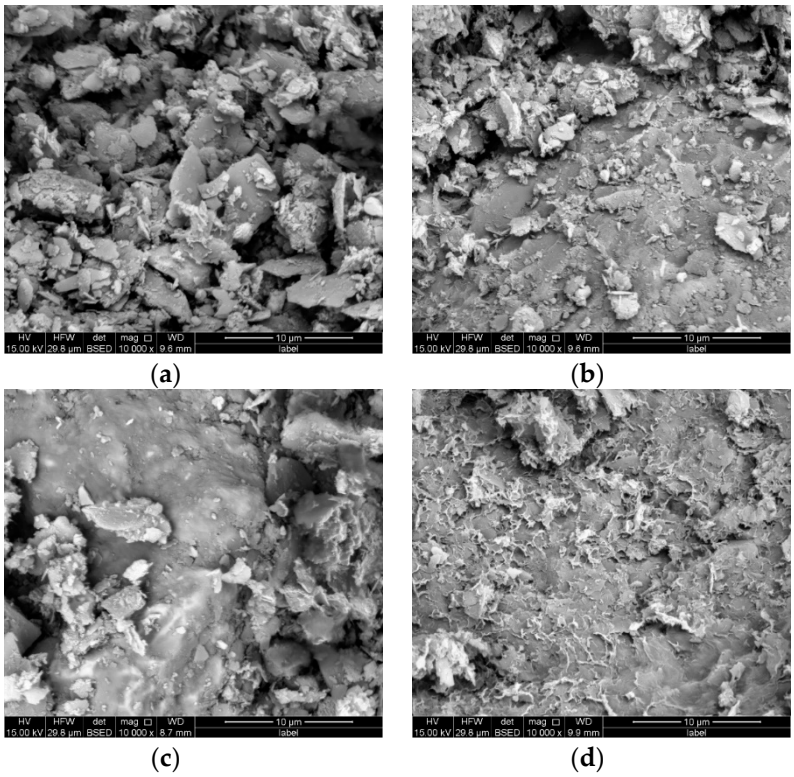


**Figure 9.** SEM micrographs for the tested samples cured for 28 days. (**a**) $A_s$ = 0 MPa; (**b**) $A_s$ = 1.2 MPa; (**c**) $A_s$ = 2.4 MPa; (**d**) $A_s$ = 3.6 MPa.

### *4.4. Passive Lateral Stress*

During the preparation of the CPB sample cured under applied stress, the CPA apparatus was used. Two strain gauges were attached outside the steel mould to estimate the passive lateral stress ($\sigma_L$) that occurred due to the presence of axial stress.

Overall the passive lateral stress increased with the increase in applied axial stress. The calculated peak passive stress in the lateral direction against different axial stresses is shown in Figure 10. As shown in Figure 10, a linear equation is suitable to analyse the increment rate of peak lateral stress (peak barricade stress) with the increase in axial applied stress (backfill stope depth). The fitted linear equation between peak lateral stress and axial applied stress can be described as follows:

$$\sigma_L = nA_s + m$$

where $n$ and $m$ are fitted coefficients.

The n = 0.2389 shows that the peak passive lateral stress is about 23.89% of the overburdened dead load in this study. A case study on the in situ axial and lateral stress measurement of CPB stope carried out by Thompson et al. showed that the lateral/horizontal stress is 20% to 50% of the actual axial stress [32]. The x-axis, axial applied stress, illustrated in the figure below, represents the total overburden load (axial applied stress) without considering the arching effect. Thompson et al. and Fahey et al. further demonstrated that the effective axial stress is about 30% to 45% of the total overburden weight due to the arching effect [32,53]. Hence, the passive lateral stress measured by the developed equipment could represent the underground barricade stress.

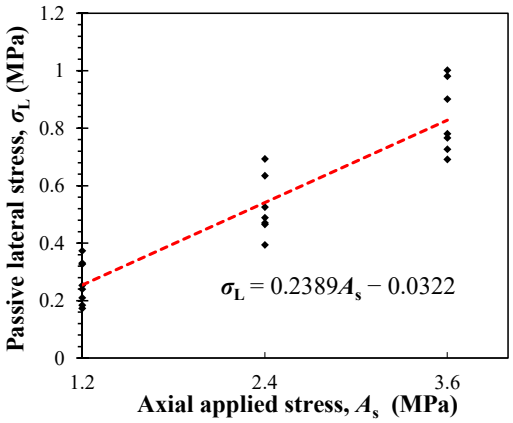


**Figure 10.** Axial applied stress ($A_s$) vs. passive lateral stress ($\sigma_L$).

## 5. Conclusions

This study presents an experimental study on the impact of axial applied stress ($A_s$) during curing on the mechanical properties of CPB material and measured the passive lateral stress during curing using a new Curing under Pressure Apparatus (CPA). Based on the results obtained, the following conclusions can be drawn from this study:

- Overall, the increase in $A_s$ during the curing period leads to higher resultant CPB peak strength and stiffness under uniaxial and triaxial compression tests; further, the influence of the curing period on CPB strength and stiffness is less notable than that of $A_s$ during curing. Moreover, the mutual effect of $A_s$ during curing kept enhancing their impact on CPB strength and stiffness, contributing to a more pronounced strength and stiffness increment at higher $A_s$ or a longer curing period.
- The CPB ductility, as represented by the axial strain at failure ($\varepsilon_f$), displays a trend in an adverse manner to what is observed for strength—with the increase in curing time and $A_s$ during curing, the samples become more brittle. Unlike the mutual enhancing influence followed for strength and stiffness, when the $A_s$ during curing increases, the curing period's effect on sample ductility becomes less sensitive.
- The axial strain at failure ($\varepsilon_f$) for all samples prepared is displayed in Figure 5a. The strain at failure is an essential index of CPB's ductility. As shown in Figure 5a, the axial strain at failure strongly depends on the curing period and $A_s$. With the increase in curing time and $A_s$ during curing, the samples become more brittle. However, unlike the trend of UCS, when the applied stress increases (i.e., to 2.4 MPa and 3.6 MPa), the influence of curing time on sample ductility become less sensitive.
- For the CPB sample cured under zero $A_s$, the SEM micrographs showed a clear visible micropore network. With the progress of the hydration process, the hydration products Calcium-Silicate-Hydrates (C–S–H), Calcium hydroxide ($Ca(OH)_2$), and ettringite (AFt) gradually fill the voids and cracks between coarse particles, contributing to the cohesion of CPB microstructure, thus developing the CPB mechanical property. The introduction of $A_s$ during curing changed the initial CPB pore structure after placement. With the increase in $A_s$, the applied stress compressed the CPB sample in macroscale, and much smaller and far fewer pores or cracks could be observed before the hydration process began. The formed hydration products could then fill the remaining voids in the CPB matric, leading to a more densely structured CPB matrix with less visible pore spaces. Furthermore, at a more extended curing period, more hydration products—especially the C–S–H calcium silicate hydrate phase—were observed in the SEM micrographs of CPB samples cured under $A_s$ than the SEM micrographs of CPB samples cured under zero $A_s$. Overall, at an early age, the increase in UCS due to axial applied stress is mainly from dense microstructures caused by the compression of tailings and cement particles. With the increase in curing time, the observation also shows that the presence of a CPB matrix with fewer pore spaces may

improve the hydration progress. Hence, the influence of axial applied stress becomes more pronounced in long-term UCS.

- The passive lateral stress measures were found at about 20% of the applied axial pressure during curing. The passive lateral stress measured may represent the stress on the barricade in an underground mine.
- With HTC Hoek triaxial as the CPB is a soft material, the CPB samples did not exhibit a detectable peak point with a rise and fall behaviour in the rock triaxial test. A soil triaxial loading machine was suggested to fail the CPB samples and detect the cohesion and friction angle for CPB samples cured under various applied stresses. Once implemented, it could improve the understanding of the influence of the self-consolidation behaviour on the mechanical properties of backfill material and benefit the engineering design of backfill stopes.

**Author Contributions:** Conceptualisation, Y.Z. and A.T.; data curation, Y.Z.; formal analysis, Y.Z.; funding acquisition, A.T. and L.G.; investigation, Y.Z.; methodology, Y.Z. and A.T.; supervision, A.T., M.K., and A.D.; validation, Y.Z.; visualisation, Y.Z.; writing—original draft, Y.Z.; writing—review and editing, A.T., M.K., A.D. and L.G.. All authors have read and agreed to the published version of the manuscript.

**Funding:** Financial support from the National Key Research and Development Program of China (2018YFE0123000) and the Key Research Fund of BGRIMM (02-1911; 02-2127) is gratefully acknowledged. This research was also partially funded by Mining Education Australia (MEA) and OZ Minerals, Australia; their support is also gratefully acknowledged.

**Acknowledgments:** The great supports and help from laboratory staff of the School of Civil, Environmental and Mining Engineering, especially Mr Adam Ryntjes and Mr Simon Golding, to this research is acknowledged.

**Conflicts of Interest:** The authors declare no conflict of interest.

## Appendix A

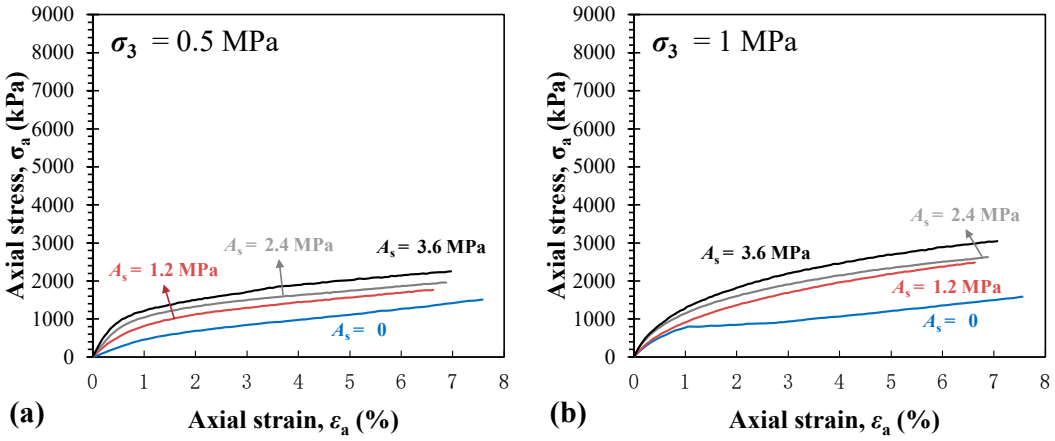

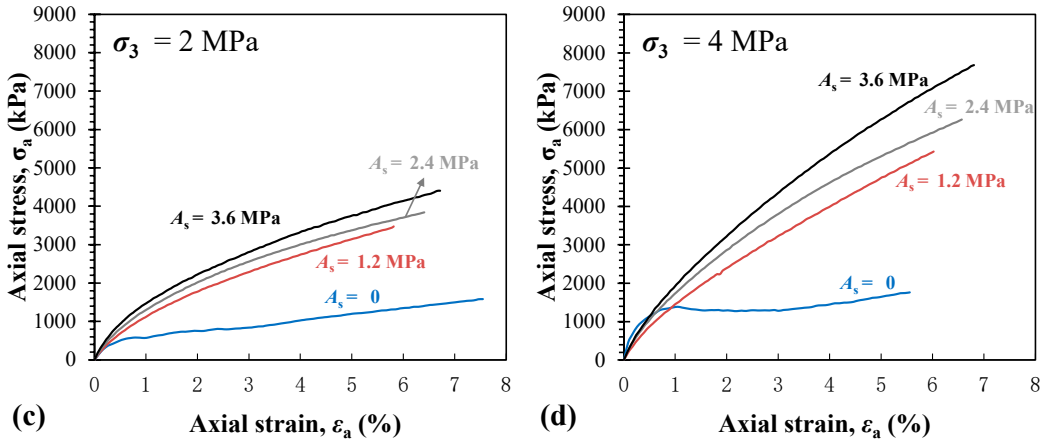


**Figure A1.** Triaxial test results for 7-day-cured samples. (**a**) stress–strain relations for $\sigma_3$ = 0.5 MPa; (**b**) stress–strain relations for $\sigma_3$ = 1 MPa; (**c**) stress–strain relations for $\sigma_3$ = 2 MPa; (**d**) stress–strain relations for $\sigma_3$ = 4 MPa.

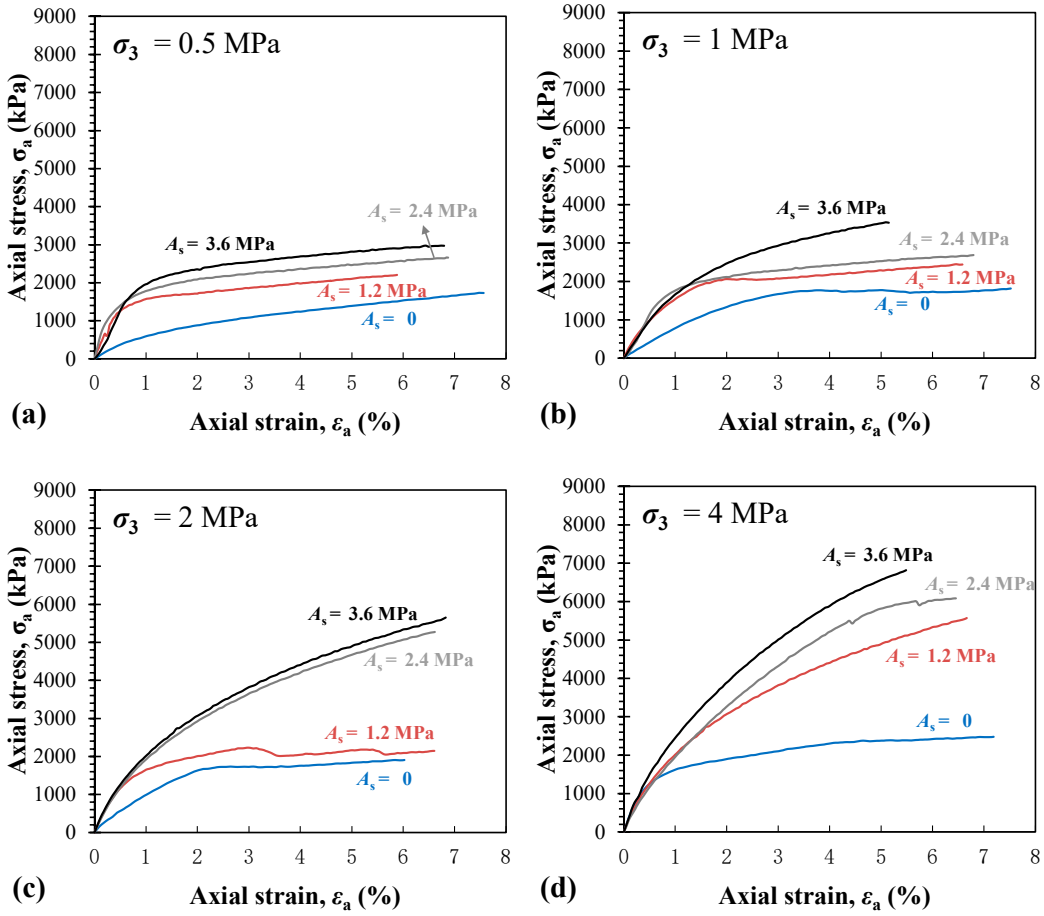


**Figure A2.** Triaxial test results for 14-day-cured samples. (**a**) stress–strain relations for $\sigma_3$ = 0.5 MPa; (**b**) stress–strain relations for $\sigma_3$ = 1 MPa; (**c**) stress–strain relations for $\sigma_3$ = 2 MPa; (**d**) stress–strain relations for $\sigma_3$ = 4 MPa.

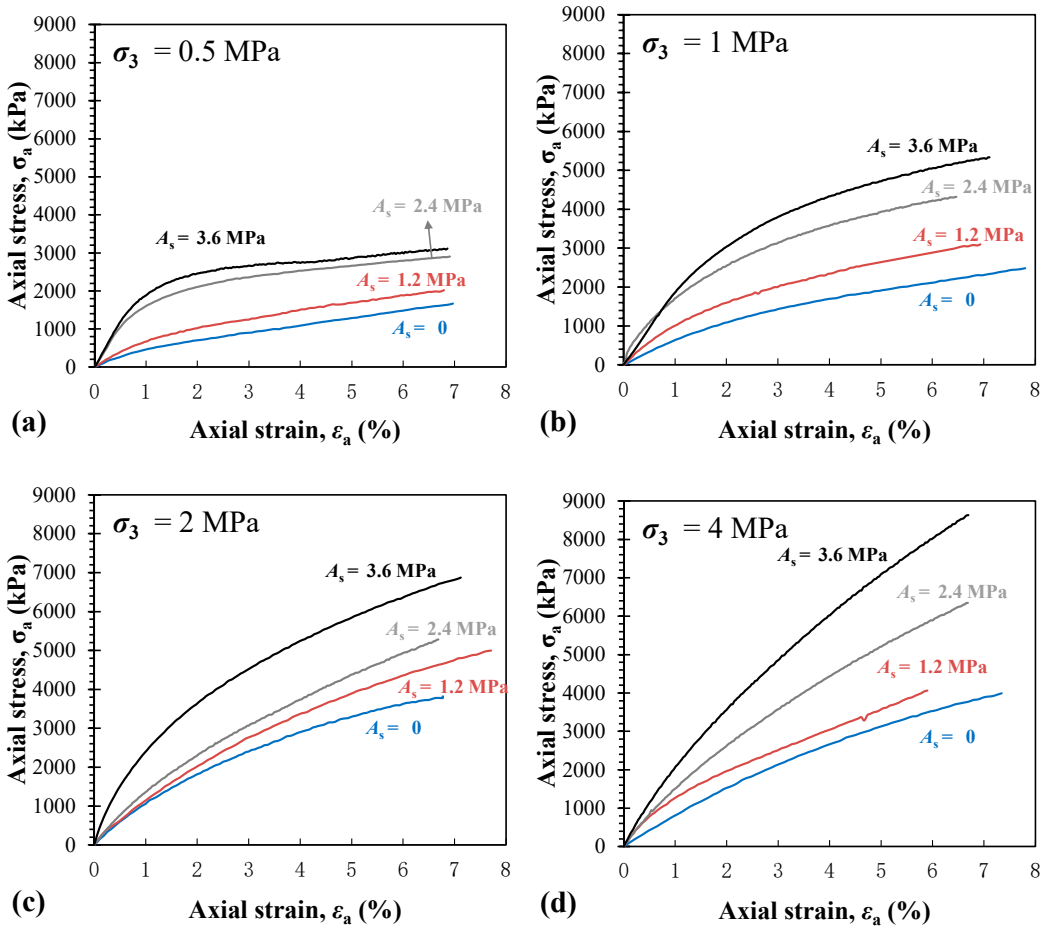


**Figure A3.** Triaxial test results for 28-day-cured samples. (**a**) stress–strain relations for $\sigma_3$ = 0.5 MPa; (**b**) stress–strain relations for $\sigma_3$ = 1 MPa; (**c**) stress–strain relations for $\sigma_3$ = 2 MPa; (**d**) stress–strain relations for $\sigma_3$ = 4 MPa.

## References


1. Jones, H.; Boger, D.V. Sustainability and Waste Management in the Resource Industries. *Ind. Eng. Chem. Res.* **2012**, *51*, 10057–10065, https://doi.org/10.1021/ie202963z.
2. Öhlander, B.; Chatwin, T.; Alakangas, L. Management of Sulfide-Bearing Waste, a Challenge for the Mining Industry. *Minerals* **2012**, *2*, 1–10, https://doi.org/10.3390/min2010001.
3. Belem, T.; Benzaazoua, M. Design and Application of Underground Mine Paste Backfill Technology. *Geotech. Geol. Eng.* **2007**, *26*, 147–174; Erratum in **2007**, *26*, 175, https://doi.org/10.1007/s10706-007-9167-y.
4. Xu, W.; Cao, P.; Tian, M. Strength Development and Microstructure Evolution of Cemented Tailings Backfill Containing Different Binder Types and Contents. *Minerals* **2018**, *8*, 167, https://doi.org/10.3390/min8040167.
5. Franks, D.; Boger, D.V.; Côte, C.M.; Mulligan, D.R. Sustainable development principles for the disposal of mining and mineral processing wastes. *Resour. Policy* **2011**, *36*, 114–122, https://doi.org/10.1016/j.resourpol.2010.12.001.
6. Tang, Y.; Zheng, J.; Guo, L.; Zhao, Y. Effect of Gypsum Addition on the Mechanical and Microstructural Performance of Sulphide-Rich Cemented Paste Backfill. *Minerals* **2021**, *11*, 283, https://doi.org/10.3390/min11030283.
7. Dold, B. Submarine Tailings Disposal (STD)—A Review. *Minerals* **2014**, *4*, 642–666, https://doi.org/10.3390/min4030642.
8. Liu, Q.; Liu, D.; Liu, X.; Gao, F.; Li, S. Research and application of surface paste disposal for clay-sized tailings in tropical rainy climate. *Int. J. Miner. Process.* **2016**, *157*, 227–235, https://doi.org/10.1016/j.minpro.2016.11.014.
9. Kesimal, A.; Yilmaz, E.; Ercikdi, B. Evaluation of paste backfill mixtures consisting of sulphide-rich mill tailings and varying cement contents. *Cem. Concr. Res.* **2004**, *34*, 1817–1822, https://doi.org/10.1016/j.cemconres.2004.01.018.
10. Kesimal, A.; Yilmaz, E.; Ercikdi, B.; Alp, I.; Deveci, H. Effect of properties of tailings and binder on the short-and long-term strength and stability of cemented paste backfill. *Mater. Lett.* **2005**, *59*, 3703–3709, https://doi.org/10.1016/j.matlet.2005.06.042.
11. Orejarena, L.; Fall, M. The use of artificial neural networks to predict the effect of sulphate attack on the strength of cemented paste backfill. *Bull. Int. Assoc. Eng. Geol.* **2010**, *69*, 659–670, https://doi.org/10.1007/s10064-010-0326-7.
12. Sivakugan, N.; Veenstra, R.; Naguleswaran, N. Underground Mine Backfilling in Australia Using Paste Fills and Hydraulic Fills. *Int. J. Geosynth. Ground Eng.* **2015**, *1*, 1–7, https://doi.org/10.1007/s40891-015-0020-8.
13. Fall, M.; Célestin, J.; Pokharel, M.; Touré, M. A contribution to understanding the effects of curing temperature on the mechanical properties of mine cemented tailings backfill. *Eng. Geol.* **2010**, *114*, 397–413, https://doi.org/10.1016/j.enggeo.2010.05.016.

14. Benzaazoua, M.; Fall, M.; Belem, T. A contribution to understanding the hardening process of cemented pastefill. *Miner. Eng.* **2004**, *17*, 141–152, https://doi.org/10.1016/j.mineng.2003.10.022.
15. Fall, M.; Pokharel, M. Coupled effects of sulphate and temperature on the strength development of cemented tailings backfills: Portland cement-paste backfill. *Cem. Concr. Compos.* **2010**, *32*, 819–828, https://doi.org/10.1016/j.cemconcomp.2010.08.002.
16. Ouattara, D.; Yahia, A.; Mbonimpa, M.; Belem, T. Effects of superplasticizer on rheological properties of cemented paste backfills. *Int. J. Miner. Process.* **2017**, *161*, 28–40, https://doi.org/10.1016/j.minpro.2017.02.003.
17. Rankine, R.M.; Sivakugan, N. Geotechnical properties of cemented paste backfill from Cannington Mine, Australia. *Geotech. Geol. Eng.* **2007**, *25*, 383–393, https://doi.org/10.1007/s10706-006-9104-5.
18. Sivakugan, N.; Rankine, R.; Rankine, K. Geotechnical considerations in mine backfilling in Australia. *J. Clean. Prod.* **2006**, *14*, 1168–1175, https://doi.org/10.1016/j.jclepro.2004.06.007.
19. Skrzypkowski, K. Compressibility of materials and backfilling mixtures with addition of solid wastes from flue-gas treatment and fly ashes. *E3S Web Conf.* **2018**, *71*, 00007, https://doi.org/10.1051/e3sconf/20187100007.
20. Ercikdi, B.; Cihangir, F.; Kesimal, A.; Deveci, H.; Alp, I. Utilization of industrial waste products as pozzolanic material in cemented paste backfill of high sulphide mill tailings. *J. Hazard. Mater.* **2009**, *168*, 848–856, https://doi.org/10.1016/j.jhazmat.2009.02.100.
21. Taheri, A.; Tatsuoka, F. Stress–strain relations of cement-mixed gravelly soil from multiple-step triaxial compression test results. *Soils Found.* **2012**, *52*, 748–766, https://doi.org/10.1016/j.sandf.2012.07.014.
22. Klein, K.; Simon, D. Effect of specimen composition on the strength development in cemented paste backfill. *Can. Geotech. J.* **2006**, *43*, 310–324, https://doi.org/10.1139/t06-005.
23. Ouellet, S.; Bussière, B.; Aubertin, M.; Benzaazoua, M. Characterization of cemented paste backfill pore structure using SEM and IA analysis. *Bull. Int. Assoc. Eng. Geol.* **2008**, *67*, 139–152, https://doi.org/10.1007/s10064-007-0117-y.
24. Fall, M.; Benzaazoua, M.; Ouellet, S. Experimental characterization of the influence of tailings fineness and density on the quality of cemented paste backfill. *Miner. Eng.* **2005**, *18*, 41–44, https://doi.org/10.1016/j.mineng.2004.05.012.
25. Zhang, J.; Li, M.; Taheri, A.; Zhang, W.; Wu, Z.; Song, W. Properties and Application of Backfill Materials in Coal Mines in China. *Minerals* **2019**, *9*, 53, https://doi.org/10.3390/min9010053.
26. Zhao, Y.; Soltani, A.; Taheri, A.; Karakus, M.; Deng, A. Application of Slag–Cement and Fly Ash for Strength Development in Cemented Paste Backfills. *Minerals* **2018**, *9*, 22, https://doi.org/10.3390/min9010022.
27. Zhao, Y.; Taheri, A.; Soltani, A.; Karakus, M.; Deng, A.; Zhao; Deng Strength Development and Strain Localization Behavior of Cemented Paste Backfills Using Portland Cement and Fly Ash. *Materials* **2019**, *12*, 3282, https://doi.org/10.3390/ma12203282.
28. Zhao, Y.; Taheri, A.; Karakus, M.; Chen, Z.; Deng, A. Effects of water content, water type and temperature on the rheological behaviour of slag-cement and fly ash-cement paste backfill. *Int. J. Min. Sci. Technol.* **2020**, *30*, 271–278, https://doi.org/10.1016/j.ijmst.2020.03.003.
29. Qin, X.; Cui, S.; Liu, L.; Wang, P.; Wang, M.; Xin, J. Prediction of Mechanical Strength Based on Deep Learning Using the Scanning Electron Image of Microscopic Cemented Paste Backfill. *Adv. Civ. Eng.* **2018**, *2018*, 1–7, https://doi.org/10.1155/2018/6245728.
30. Aldhafeeri, Z.; Fall, M.; Pokharel, M.; Pouramini, Z. Temperature dependence of the reactivity of cemented paste backfill. *Appl. Geochem.* **2016**, *72*, 10–19, https://doi.org/10.1016/j.apgeochem.2016.06.005.
31. Le Roux, K.; Bawden, W.F.; Grabinsky, M.F. Field properties of cemented paste backfill at the Golden Giant mine. *Min. Technol.* **2005**, *114*, 65–80, https://doi.org/10.1179/037178405x44557.
32. Thompson, B.; Bawden, W.; Grabinsky, M. In situ measurements of cemented paste backfill at the Cayeli Mine. *Can. Geotech. J.* **2012**, *49*, 755–772, https://doi.org/10.1139/t2012-040.
33. Yilmaz, E.; Benzaazoua, M.; Belem, T.; Bussière, B. Effect of curing under pressure on compressive strength development of cemented paste backfill. *Miner. Eng.* **2009**, *22*, 772–785, https://doi.org/10.1016/j.mineng.2009.02.002.
34. Belem, T.; El Aatar, O.; Bussiere, B.; Benzaazoua, M.; Fall, M.; Yilmaz, E. Characterisation of Self-Weight Consolidated Paste Backfill. In *Paste 2006: Proceedings of the Ninth International Seminar on Paste and Thickened Tailings*; Jewell, R., Lawson, S., Newman, P., Eds.; Australian Centre for Geomechanics: Perth, Austrilia, 2006; pp. 335–345.
35. Grabinsky, M.; Bawden, W.F.; Simon, D.; Thompson, B. In situ properties of cemented paste backfill in an Alimak Stope. In Proceedings of the 61st Canadian Geotechnical Conference and 9th Joint CGS/IAH-CNC Groundwater Conference; Edmonton, Alberta, Canada, 21–24 September 2008.
36. le Roux, K.-A.; Bawden, W.F.; Grabinsky, M.W.F. Comparison of the material properties of in situ and laboratory prepared cemented paste backfill.In Proceedings of the The 104th CIM Annual Conference, Vancouver, BC, Canada, 28 April–1 May 2002; pp. 201–209.
37. Benzaazoua, M.; Belem T.; Yilmaz,E. Novel lab tool for paste backfill. *Can. Min. J.* **2006**, *127*, 31–33.
38. Yilmaz, E. One-Dimensional Consolidation Parameters of Cemented Paste Backfills / Parametry Jednowymiarowej Konsolidacji Podsadzki W Postaci Cementowej Pasty. *Gospod. Surowcami Miner. - Miner. Resour. Manag.* **2012**, *28*, 29–45, https://doi.org/10.2478/v10269-012-0030-2.
39. Yilmaz, E.; Belem, T.; Bussière, B.; Benzaazoua, M. Relationships between microstructural properties and compressive strength of consolidated and unconsolidated cemented paste backfills. *Cem. Concr. Compos.* **2011**, *33*, 702–715, https://doi.org/10.1016/j.cemconcomp.2011.03.013.
40. Yilmaz, E.; Belem, T.; Benzaazoua, M. Effects of curing and stress conditions on hydromechanical, geotechnical and geochemical properties of cemented paste backfill. *Eng. Geol.* **2014**, *168*, 23–37, https://doi.org/10.1016/j.enggeo.2013.10.024.

41. Sivakugan, N.; Widisinghe, S. Stresses Within Granular Materials Contained Between Vertical Walls. *Indian Geotech. J.* **2012**, *43*, 30–38, https://doi.org/10.1007/s40098-012-0029-z.
42. Sobhi, M.A.; Li, L. Numerical investigation of the stresses in backfilled stopes overlying a sill mat. *J. Rock Mech. Geotech. Eng.* **2017**, *9*, 490–501, https://doi.org/10.1016/j.jrmge.2017.01.001.
43. A Take, W.; Valsangkar, A.J. Earth pressures on unyielding retaining walls of narrow backfill width. *Can. Geotech. J.* **2001**, *38*, 1220–1230, https://doi.org/10.1139/cgj-38-6-1220.
44. ASTM D4318-00. *Standard Test Methods for Liquid Limit, Plastic Limit, and Plasticity Index of Soils;* ASTM International: West Conshohocken, PA, USA, 2000.
45. ASTM D698-12. *Standard Test Methods for Laboratory Compaction Characteristics of Soil Using Standard Effort (12,400 ft-lbf/ft3 (600 kN-m/m3))* ASTM International: West Conshohocken, PA, USA, 2012.
46. ASTM C39/C39M-21. *Standard Test Method for Compressive Strength of Cylindrical Concrete Specimens*; ASTM International: West Conshohocken, PA, USA, 2021.
47. ASTM D2664-95a. *Standard Test Method for Triaxial Compressive Strength of Undrained Rock Core Specimens without Pore Pressure Measurements*; ASTM International: West Conshohocken, PA, USA, 1995.
48. Zhang, B.; Xin, J.; Liu, L.; Guo, L.; Song, K.-I. An Experimental Study on the Microstructures of Cemented Paste Backfill during Its Developing Process. *Adv. Civ. Eng.* **2018**, *2018*, 1–10, https://doi.org/10.1155/2018/9783046.
49. Koohestani, B.; Koubaa, A.; Belem, T.; Bussière, B.; Bouzahzah, H. Experimental investigation of mechanical and microstructural properties of cemented paste backfill containing maple-wood filler. *Constr. Build. Mater.* **2016**, *121*, 222–228, https://doi.org/10.1016/j.conbuildmat.2016.05.118.
50. Chen, X.; Shi, X.; Zhou, J.; Chen, Q.; Li, E.; Du, X. Compressive behavior and microstructural properties of tailings polypropylene fibre-reinforced cemented paste backfill. *Constr. Build. Mater.* **2018**, *190*, 211–221, https://doi.org/10.1016/j.conbuildmat.2018.09.092.
51. Niroshan, N.; Yin, L.; Sivakugan, N.; Veenstra, R.L. Relevance of SEM to Long-Term Mechanical Properties of Cemented Paste Backfill. *Geotech. Geol. Eng.* **2018**, *36*, 2171–2187, https://doi.org/10.1007/s10706-018-0455-5.
52. Schreier, H.; Orteu, J.-J.; Sutton, M.A. *Image Correlation for Shape, Motion and Deformation Measurements*; Springer: Boston, MA, USA, 2009, https://doi.org/10.1007/978-0-387-78747-3.
53. Fahey, M.; Helinski, M.; Fourie, A. Development of Specimen Curing Procedures that Account for the Influence of Effective Stress During Curing on the Strength of Cemented Mine Backfill. *Geotech. Geol. Eng.* **2011**, *29*, 709–723, https://doi.org/10.1007/s10706-011-9412-2.